The Ocean Boundary Layer below Hurricane Dennis

ERIC A. D'ASARO

Applied Physics Laboratory and School of Oceanography, University of Washington, Seattle, Washington

(Manuscript received 4 February 2002, in final form 3 September 2002)

ABSTRACT

Three neutrally buoyant floats were air deployed ahead of Hurricane Dennis on 28 August 1999. These floats were designed to accurately follow three-dimensional water trajectories and measure pressure (i.e., their own depth) and temperature. The hurricane eye passed between two of the floats; both measured the properties of the ocean boundary layer beneath sustained 30 m s^{-1} winds. The floats repeatedly moved through a mixed layer 30–70 m deep at average vertical speeds of 0.03–0.06 m s^{-1}. The speed was roughly proportional to the friction velocity. Mixed layer temperature cooled about 2.8° and 0.75°C at the floats on the east and west sides of the northward-going storm, respectively. Much of the cooling occurred before the eye passage. The remaining terms in the horizontally averaged mixed layer heat budget, the vertical velocity–temperature covariance and the Lagrangian heating rate, were computed from the float data. Surface heat fluxes accounted for only a small part of the cooling. Most of the cooling was due to entrainment of colder water from below and, on the right-hand (east) side only, horizontal advection and mixing with colder water. The larger entrainment flux on this side of the hurricane was presumably due to the much larger inertial currents and shear. Although these floats can make detailed measurements of the heat transfer mechanisms in the ocean boundary layer under these severe conditions, accurate measurements of heat flux will require clusters of many floats to reduce the statistical error.

1. Introduction

Hurricanes draw their energy from the sensible and latent heat supplied by warm ocean waters. Their intensity is therefore highly sensitive to the sea surface temperature (SST). Emanuel (1999) notes that

> . . . there has been . . . little advance in predictions of [hurricane] intensity (as measured, for example, by maximum surface wind speed), in spite of the application of sophisticated numerical models. The best intensity forecasts today are statistically based. Most of the research literature on hurricane intensity focusses on the pre-storm sea surface temperature and certain properties of the atmospheric environment. . . . This remains so, even though it is well known that hurricanes alter the surface temperature of the ocean over which they pass and that a mere 2.5 K decrease in ocean surface temperature near the core of the storm would suffice to shut down energy production entirely. Simulations with coupled atmosphere–ocean models confirm that interaction with the ocean is a strong negative feedback on storm intensity.

Cooling of the upper ocean by hurricanes, or the lack thereof, is important to hurricane dynamics and prediction. The cooling results primarily from the mixing of cold deep water into the mixed layer (Price et al. 1994; Jacob et al. 2000). The mixing is caused by strong shears in the upper ocean forced by the hurricanes winds. Emanuel (1999) shows that simple models of hurricane intensity that include this feedback produce greatly improved predictions compared to those that do not.

Despite this, there are only a few observations of the upper ocean beneath a hurricane. Such measurements are difficult to make due to the large surface waves, winds, and currents, as well as the highly intermittent and unpredictable locations of hurricanes. Targeted studies (Sanford et al. 1987; Shay et al. 1992) have generally used air-deployed profilers. Other measurements have resulted from long-term observations that have been fortuitously overrun by hurricanes (e.g., Dickey et al. 1998). Here, we describe the first use of air-deployed neutrally buoyant floats to observe mixing beneath a hurricane.

Another major uncertainty in hurricane prediction results from the poor understanding of air–sea heat fluxes at high winds. Extrapolation of existing parameterizations to hurricane force winds results in heat fluxes that are insufficient to sustain a hurricane (Emanuel 1999). The additional fluxes may result from the evaporation of spray (Andreas 1998). Direct measurements of air–sea fluxes under hurricane conditions on the air side of the interface may be difficult, particularly because sensible, latent, and spray components must be measured. Here, we report on heat flux measurements made on the water side of the interface.

Corresponding author address: Dr. Eric A. D'Asaro, Applied Physics Laboratory, University of Washington, 1013 NE 40th St., Seattle, WA 98105.
E-mail: dasaro@apl.washington.edu

Furthermore, the hurricane environment offers a unique opportunity to study the physics of upper-ocean turbulence. This is important because turbulence in the ocean boundary layer is forced by a combination of wind stress, surface waves, surface buoyancy flux, and shear. However, it is often difficult to separate the effects of waves from those of wind because the wave properties are often highly correlated with the wind. Hurricane winds change in both magnitude and direction so rapidly that the surface waves are far from equilibrium (Wright et al. 2001). Furthermore, the hurricane forcing is so strong that the effects of preexisting oceanic currents and swell on the boundary layer turbulence are diminished. Under these conditions, it may be much easier to untangle the interactions between wind, waves, and upper-ocean turbulence. This paper presents initial steps toward this goal.

Section 2 describes the Lagrangian floats used in these measurements, and the methods by which air–sea fluxes were estimated from operational hurricane data. Section 3 describes Hurricane Dennis and the basic properties of turbulence observed beneath it. Section 4 describes the methods of extracting heat flux profiles from Lagrangian float data. Section 5 applies these methods to the data to produce estimates of the surface and entrainment heat fluxes. Section 6 places these observations in the context of the issues raised above and summarizes the results.

2. Instrumentation and methods

a. Lagrangian floats

Measurements of water trajectories and the temperature along these trajectories were made using high-drag, neutrally buoyant floats [Deep Lagrangian Floats (DLFs)] constructed at the Applied Physics Laboratory, University of Washington. D'Asaro (2003, hereinafter DAS) describes the construction and performance of these floats in detail. Three floats were air-deployed ahead of the hurricane and gathered data for 4 days. Pressure was measured every 20 s with an accuracy of 0.1 dbar from which depth, vertical velocity, and acceleration were computed. Temperature was measured every 20 s to an accuracy of approximately 1 mK using the electronics and thermistor from a Seabird CTD. At the end of the mission, the floats dropped a weight, surfaced, and relayed their data via the ARGOS satellite system.

Data packets, once converted to pressure and temperature data, required little additional processing. A small number of missing data points were linearly interpolated onto the 20-s sampling grid. The measured pressure was corrected for the changes in atmospheric pressure associated with the hurricane; these corrections are small, about 0.4 dbar at the most, but significant when examining float trajectories very near the surface.

Turbulent velocity fluctuations in the oceanic boundary layer under a hurricane are many centimeters per second, much smaller than the meter per second velocities of the surface waves. This presents a formidable measurement challenge. However, because pressure fluctuations are zero along particle paths for linear surface waves and surface waves are nearly linear, the surface wave pressure fluctuations measured by Lagrangian floats are greatly attenuated from their Eulerian values (D'Asaro et al. 1996; D'Asaro 2001). This allows accurate measurements of vertical velocity to be made from pressure measured on Lagrangian floats.

These floats are not perfectly Lagrangian; they do not follow water parcels exactly. There are two major sources of error. First, the floats are not perfectly neutrally buoyant. For the first day after the float is deployed it adjusts its buoyancy to make itself neutrally buoyant in the mixed layer (see DAS for a detailed discussion). Scientific data collection starts only after this operation is complete. Even if the floats are exactly neutral when they first enter the mixed layer, the rapid cooling of the mixed layer during the hurricane will cause them to become lighter. A 2°C cooling will produce about 8 g of buoyancy. The float compensates for this effect using the measured temperature and the known expansion coefficients of seawater and its aluminum hull. It cannot compensate for changes in the mixed layer density due to salinity caused, for example, by entrainment of water into the mixed layer.

Typical float buoyancies are a few grams. The effect of this buoyancy on the float motion is greatly reduced by a circular cloth drogue with a frontal area of about 1 m^2. With the drogue open, a buoyancy of 5 g results in an upward motion of 5 mm s^{-1} relative to the water assuming a quadratic drag law (DAS). Without measurements more detailed than are available on a DLF, the buoyancy of a float cannot be directly determined. However, light floats tend to concentrate near the ocean surface; heavy floats tend to concentrate near the bottom of the mixed layer. Therefore, the histogram of float depth can be used as a diagnostic for the float buoyancy (DAS).

The second major source of float error results from the approximately 1-m size of the float. This is much larger than the smallest scales of turbulence but smaller than the largest scales, which are comparable to those of the mixed layer itself. The float's finite size reduces its response to velocity fluctuations smaller than itself as quantified by Lien et al. (1998). Fortunately, the larger scales contain most of the energy so that the float measures vertical velocity accurately as long as the mixed layer is substantially larger than the float size. This is probably also true for vertical fluxes, although this is less well quantified.

A similar error results from the placement of the pressure and temperature sensors on the top of the float, approximately 0.3 m above the center of buoyancy and 0.6 m above the drogue. These sensors therefore do not

follow a Lagrangian trajectory even if the center of the float does.

b. Hurricane Dennis deployments

Hurricane Dennis was the third hurricane of the 1999 season (Lawrence et al. 2001). It was a larger-than-average hurricane with a large and poorly formed eye structure (Fig. 1). It formed over the eastern Bahamas on 24 August and reached hurricane strength on the 26th. Maximum strength (90 kts, 962 hPa) occurred 28–30 August as Dennis moved northward just east of Florida. The storm then turned northeast, stalling off North Carolina and making landfall on 4 September.

Three Lagrangian floats were deployed between 2200 and 2300 UTC 27 August 1999 ahead of Hurricane Dennis using a chartered King Air skydiving aircraft. The storm was forecast to travel north along 79°W. The three floats were therefore deployed in a line centered on 79°W; the actual track was about 1° east of the forecast. The eye of the storm passed between the deployment locations of floats 36 and 37. There is no additional information on the floats' positions until they surfaced four days later.

c. Air–sea fluxes

1) DATA

Air–sea fluxes were computed using bulk formulas and operational surface wind speed maps produced by the Hurricane Research Division of the National Oceanic and Atmospheric Administration using observations from ships, moored buoys, and research aircraft flight level and dropsonde winds (Powell et al. 1998). Wind speed contours from each map were hand-digitized and bilinearly interpolated in space. An example of the resulting wind speed map is shown in Fig. 1. Wind direction at a given location in these maps was found to be very close to 112.6° counterclockwise from the center of the storm. This constant turning angle is undoubtedly an artifact of the Powell et al. (1998) mapping scheme, but was used nevertheless. The vector wind was therefore computed using the interpolated wind speed and the computed direction. Vector surface winds at other times were computed by linearly interpolating in time between values computed from the two nearest maps after correcting for the motion of the storm.

2) BULK FORMULAS

Wind stress was computed from the surface wind using the Large and Pond (1981) neutral drag coefficient. Price et al. (1994) found that this drag law produced modeled mixed currents in reasonable agreement with the observations from three hurricanes. The drag law error is probably at least 20%.

Sensible heat flux Q_h was computed using the bulk expression

$$Q_h = C_h U \Delta T \rho_{\text{air}} C_p, \tag{1}$$

where U is the wind speed, ρ_{air} is the density of air, C_p is its heat capacity, and $C_h = 1 \times 10^{-3}$ is the transfer coefficient. Note that Price et al. (1996) use $C_h = 1.3 \times 10^{-3}$ while Jacob et al. (2000) use $C_h = 1 \times 10^{-3}$. There are no direct measurements of ΔT, the air–sea temperature difference. Cione et al. (2000) compile data from many hurricanes and find the average $\Delta T = 2.5 \pm 1.5$°C within a few degrees of the storm center. Price et al. (1994) use 3°C. The average values from Cione et al. (2000) are used in (1).

Latent heat flux Q_l was computed using the bulk expression

$$Q_l = C_h U \Delta q \rho_{\text{air}} L, \tag{2}$$

where L is the latent heat of evaporation and $C_h = 1.2 \times 10^{-3}$ is the transfer coefficient. Note that Price et al. (1994) and Jacob et al. (2000) both use $C_h = 1.3 \times 10^{-3}$. There are no direct measurements of Δq, the difference between surface humidity and saturation humidity. Cione et al. (2000) find that the relative humidity is close to saturation (97%) near the storm center and decreases to 85% at 4° from the center. An interpolated version of this profile is used to compute Δq. This results in about 30% less latent heat flux than if a constant 85% relative humidity is assumed.

Andreas (1998) argues that the evaporation of wind-blown spray will make large contributions to the sensible and latent heat fluxes at high wind speeds. The resulting sensible and latent heat fluxes are proportional to ΔT and Δq, respectively, but have a much stronger dependence on wind speed than that used in (1) and (2). These spray fluxes can therefore not be parameterized using (1) and (2). Estimates of the spray fluxes were computed based on a fit to the figures in Andreas (1998):

$$Q_{hs} = 40\left(\frac{U}{32}\right)^5 \Delta T \qquad [\text{W m}^{-2}], \tag{3}$$

$$Q_{ls} = 790\left(\frac{U}{32}\right)^5 \frac{1 - R}{1 - 0.8} \quad [\text{W m}^{-2}], \tag{4}$$

where R is the relative humidity. Equation (4) uses the relationship $\Delta q \sim (1 - R)$ to extrapolate the 80% humidity in Andreas (1998) to other relative humidities. The latent heat flux is much larger than the sensible heat flux. Comparison with a more recent parameterization indicates that (3) and (4) may overestimate the spray fluxes (E. Andreas 2002, personal communication). Thus the correct heat flux probably lies between that computed using the sum of (1), (2), (3), and (4) and that computed using only the sum of (1) and (2).

3) INERTIAL CURRENTS AND FLOAT POSITIONING

Although the floats' positions are known only at the float launch time and from ARGOS fixes starting 4 days later, these plus modeled hurricane currents constrain

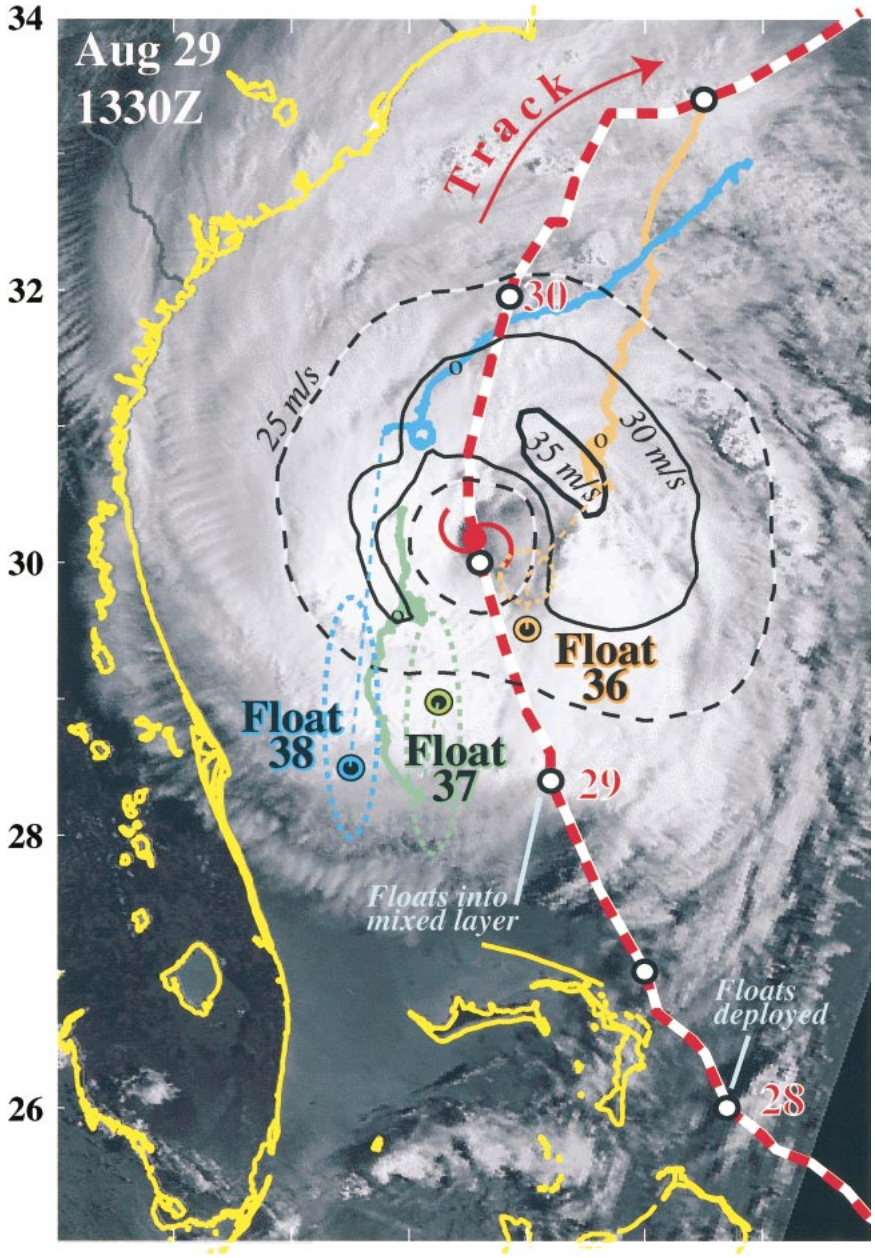

FIG. 1. AVHRR image of Hurricane Dennis at 1338 UTC 29 Aug 1999 (image provided by Ocean remote sensing group, The Johns Hopkins University, Applied Physics Laboratory). The image is annotated with the hurricane center at 1330 UTC, the coastline of southeastern United States and the Bahamas (yellow), the track of Hurricane Dennis (red) with circles every 12 h, wind speed contours from the NOAA/AOML/HRD wind analysis at 1330 UTC, and the deployment location (colored circles) of each Lagrangian float. The floats were deployed 2200–2300 UTC 28 Aug, began making measurements in the mixed layer at approximately 0000 UTC 29 Aug, and surfaced early on 1 Sep. The ARGOS locations of the floats after surfacing are shown color coded for each float. The black ''o'' on each track marks the float position 4 days after surfacing. The dashed, color-coded ellipses show the estimated uncertainty (1 std dev) of the float position at 1330 UTC.

the possible float trajectories. In the end, however, the errors in the float position remain large and cause large uncertainties in the estimated air–sea fluxes.

The wind stress was used to force a slab mixed layer model (Pollard and Millard 1970; D'Asaro 1985) with a fixed layer depth H. The wind stress near float 36, on the east side of the storm, rotated clockwise with time at a rate nearly resonant at the inertial frequency. With $H = 100$ m, the model predicts 1.2–1.5 m s^{-1} inertial current amplitudes and 17–22-km inertial displacement

amplitudes. These are comparable to the mixed layer inertial currents observed in similar hurricanes (Price et al. 1994; Jacob et al. 2000). Float 36 underwent inertial oscillations of about 5-km amplitude after it surfaced; these decayed with a half-life of 2 days. Boldly extrapolating back to 29 August yields wind-forced inertial oscillations of about 20-km amplitude, consistent with the model. This model guidance thus has float 36 executing a near circle under the influence of the hurricane winds, with a 20-km diameter starting to the northwest and ending about 10 km east of its starting position.

Floats 37 and 38 were on the east side of the hurricane where the winds rotated anticlockwise with time. There was no inertial resonance and the inertial amplitudes after surfacing were about half those seen at float 36 and showed about the same decay timescale. The model predicts horizontal displacements of about 10 km south to southwest for float 37, with the direction dependent on the exact location of the float, and about 10 km southwest for float 38.

Based on these estimates and the variability of the float track after surfacing, the best-guess position of each float during the storm passage was taken as the deployment position plus 1.5 days of advection at the mean of the average velocity from deployment to surfacing and the average velocity during the first 3 days after surfacing plus a small additional displacement to represent the wind-forced motions: for float 36, 13 km northward and 11 km westward; for floats 37 and 38, 8 km southward and westward. The uncertainty is estimated from the variability of the float trajectories after surfacing. It is modeled as a Gaussian with 0.2° standard deviation in both latitude and longitude for all floats except for a 0.9° standard deviation in the latitude uncertainty for floats 37 and 38. The resulting spread of float positions are shown in Fig. 1. Estimates of the air–sea fluxes and their errors are shown in Fig. 2.

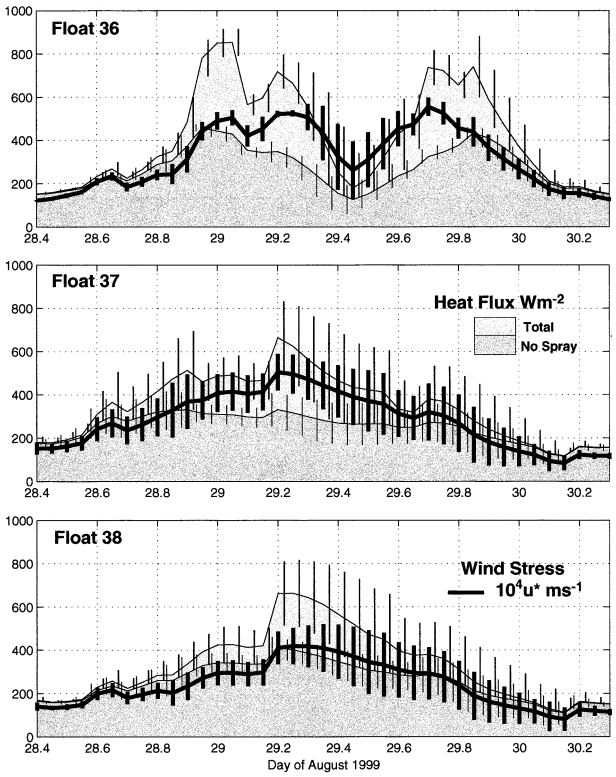

FIG. 2. Heat flux and friction velocity in the ocean ($\times 10^4$) at each float computed from NHC operational maps, bulk formulas and estimated float position. Two heat flux curves are shown: a lower one showing the sum of sensible and latent heat fluxes computed using the usual bulk formulas, and an upper one showing the effect of this plus sensible and latent heat fluxes due to spray. Error bars show one standard deviation due to uncertainty in float position. There is additional uncertainty due to errors in the atmospheric wind, temperature, humidity, and in the bulk formulas.

3. Data overview

Figure 3 shows pressure and potential temperature for all three floats. Floats repeatedly cycled across a layer 20–50 m deep thus defining the layer of near-surface turbulence and rapid mixing. Typical vertical velocities were 0.02–0.06 m s^{-1}; maximum vertical velocities were about 0.2 m s^{-1}. Section 5a examines the statistics of vertical velocity in more detail.

The mixing layer defined by the float trajectories was nearly isothermal and was thus very similar to the mixed layer defined by temperature. The dashed line in Fig. 3 shows the estimated layer depth based on the float trajectories and temperature. The temperature of the mixed layer for all three floats decreased with time, but the magnitude of the decrease varied from almost 3°C at float 36, to about 1°C at float 37, to about 0.8°C at float 38. This is consistent with previous hurricane observations and models (Price et al. 1994; Jacob et al. 2000) showing that the strong inertial currents on the right-hand side of a hurricane (float 36) lead to much stronger shears, mixing, upward entrainment of colder water, and thus much more cooling of the mixed layer.

Figure 4 shows a potential temperature/depth trajectory for an approximately 1-h segment of data from float 36. If the float is Lagrangian, changes in the measured temperature are due to heating or cooling of the water parcel being tracked. This allows a simple diagnosis of the processes of heat transport (Fig. 4). The float usually cooled when it encountered the bottom of the mixed layer (segments CD and H); this is the entrainment heat flux. It also cooled near the surface (B and G); this is the surface heat flux. While transiting the mixed layer, the float temperature sometimes remained the same (segment BC); this is vertical heat transport. Sometimes, however, strong cooling occurred within the mixed layer (segment EF); this cannot be the result of vertical processes because there are no significant heat sources within the ocean interior and therefore must represent horizontal mixing. Section 5b quantifies these various heat transport processes.

The occasional deep excursions of floats below the

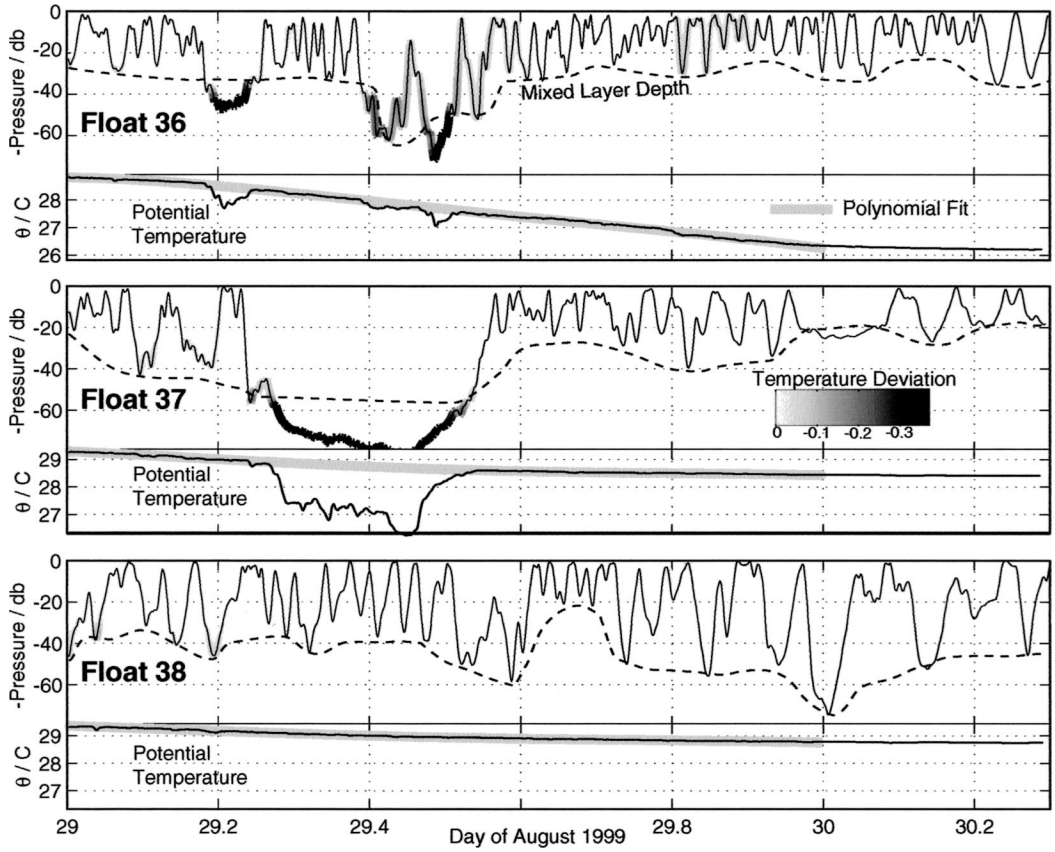

FIG. 3. Potential temperature and pressure data for all three floats. Bottom panel for each float shows potential temperature; thick shaded line shows polynomial fit to all points with depths shallower than 30 m. Top panel for each float shows pressure; thick shading indicates deviation of temperature from polynomial fit; the shading for temperature deviations less than about 0.05°C is white and invisible. The dashed line shows the estimated mixing layer depth based on the depth of float excursions and the temperature deviations. The figure axes are the same for all three floats except for an offset in temperature.

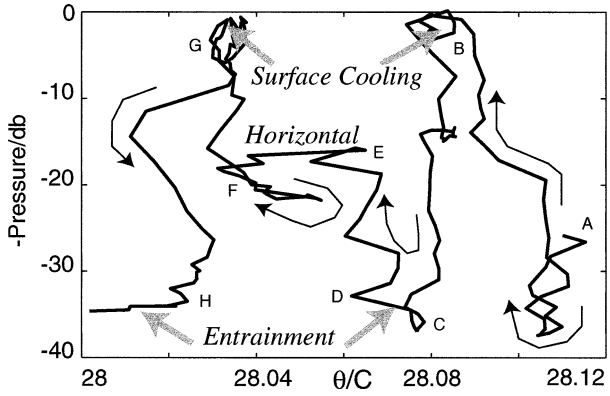

FIG. 4. Potential temperature/depth trajectory of float 36 during an approximately 1-h period. The water cools at the surface, at the bottom of the trajectories (entrainment), and in occasional middepth events (horizontal mixing).

mixed layer (Fig. 3) are probably due to the float improperly making itself denser than the mixed layer. This can occur because the floats correct for density changes due to temperature, but cannot correct for salinity changes. DAS discusses this in more detail.

4. Analysis methods

a. Goals and limitations

The temperature, pressure, and vertical velocity data from the floats were used to generate a variety of statistics on the properties of the turbulence in the mixed layer beneath Hurricane Dennis. However, the amount of data was quite limited; the hurricane passed over the floats in about a day, the meteorological fluxes were not constant during this time and the floats spent some of this time beneath the mixed layer. The number of degrees of freedom for these statistics is governed by the number of times that a float transits the mixed layer; this was only 30–50 for each float during the hurricane passage. Thus, at best, average profiles of various sta-

tistics could be computed and even these had large error bars. Consistency tests between different quantities were used to check for gross errors due to statistical problems or methodological biases.

b. Vertical velocity

The vertical acceleration can be written

$$\frac{Dw}{Dt} = \frac{\partial w}{\partial t} + \frac{1}{2}\frac{\partial w^2}{\partial z} + \nabla_H \cdot (uw), \tag{5}$$

where ∇_H is the horizontal gradient operator. Averaging this in time and horizontally so the second and last terms vanish yields

$$\left\langle \frac{Dw}{Dt} \right\rangle (z) = \frac{\partial}{\partial z}\left\langle \frac{w^2}{2} \right\rangle (z), \tag{6}$$

where the $\langle\ \rangle$ denotes the averaging operation. Thus the profile of $\langle w^2 \rangle(z)$ can be computed either directly, which will be denoted as σ_w^2, or from

$$\langle w^2 \rangle(z) = 2\int_z^0 \left\langle \frac{Dw}{Dt} \right\rangle (z)\, dz, \tag{7}$$

where $w = 0$ at $z = 0$, which will be denoted as σ_{wA}^2. The comparison of σ_w^2 and σ_{wA}^2 provides a test of the accuracy of the measurements and of the horizontal averaging. Harcourt et al. (2002) shows an example of this in a numerical simulation.

c. Heat flux—Eulerian perspective

The potential temperature equation can be written

$$\frac{D\theta}{Dt} = \frac{\partial \theta}{\partial t} + \frac{\partial w\theta}{\partial z} + \nabla_H \cdot (u\theta). \tag{8}$$

Averaging this in time and horizontally, but allowing for the possibility of a temperature trend yields

$$\left\langle \frac{\partial \theta}{\partial t} \right\rangle (z) = -\frac{\partial \langle w\theta \rangle}{\partial z}(z) + \left\langle \frac{D\theta}{Dt} \right\rangle (z). \tag{9}$$

The terms are, in order, the Eulerian heating rate, the vertical divergence of the advective flux, and the Lagrangian heating rate.

Letting H denote the depth to which the heat budget is to be computed, the mixed layer temperature is

$$\overline{\Theta_{\rm ml}} = \frac{1}{H}\int_{-H}^0 \langle \theta \rangle\, dz. \tag{10}$$

If $\overline{\Theta_{\rm ml}}$ is steadily changing it is more useful to rewrite the advective heat flux in (9) using $\theta' = \theta - \overline{\Theta}_{\rm ml}$ since its statistics are more stationary. Define the advective heat flux

$$\Phi_A(z) \equiv \langle w\theta \rangle(z) = \langle w\theta' \rangle(z), \tag{11}$$

since $\overline{\Theta}_{\rm ml}$ is a constant at any given time and $\langle w \rangle = 0$. Define the diffusive flux

$$\Phi_D(z) \equiv \int_z^0 \left\langle \frac{D\theta}{Dt} \right\rangle dz. \tag{12}$$

The heat equation (9), integrated from $z = 0$, can therefore be written

$$\overline{\Theta}_t z = \Phi_A(z) + \Phi_D(z), \tag{13}$$

where

$$\overline{\Theta}_t \equiv \frac{d\overline{\Theta}_{\rm ml}}{dt}, \tag{14}$$

where $w = 0$ at the surface and θ is assumed to equal $\Theta_{\rm ml}$. Equation (13) can be written as a flux divergence,

$$\overline{\Theta}_t = \frac{\partial}{\partial z}[\Phi_A(z) + \Phi_D(z)], \tag{15}$$

so that the total vertical flux is the sum of the advective Φ_A and diffusive Φ_D components.

The Lagrangian heat equation is

$$\frac{D\theta}{Dt} = \kappa \nabla^2 \theta, \tag{16}$$

where the difference between real and potential temperature has been ignored. At the surface, $w = 0$ so $\Phi_A = 0$. The surface heat flux is entirely diffusive:

$$\frac{Q_0}{\rho C_p} \equiv \lim_{z\to 0}\left[\left\langle \kappa \frac{\partial \rho}{\partial z} \right\rangle\right] = \lim_{z\to 0} \Phi_D(z), \tag{17}$$

where ρC_p converts temperature flux (m s^{-1} °C) to heat flux (W m^{-2}). D'Asaro et al. (2002) show, using a simulated boundary layer, that the limit in (17) is nearly singular; $\Phi_D(z)$ increases very rapidly in a near-surface boundary layer of width δ_s. The surface heat flux is evaluated just outside this boundary layer:

$$Q_{0D} = \lim_{z\to 0;\, z>-\delta_s} \Phi_D(z)\rho C_p \tag{18}$$

defines the surface heat flux evaluated from Φ_D. Corrections for the finite size of δ_s/H may also be necessary, hence the retention of the limit notation in (18). Practically, this limit is evaluated by a linear fit to Φ_D in a region away from the boundary layer, which is extrapolated to $z = 0$.

In the interior of the mixed layer, the diffusive flux is small; all the flux is advective. The flux at $z = -H$, the entrainment flux, evaluated from Φ_A, is

$$Q_{\rm EA} = \Phi_A(-H)\rho C_p \tag{19}$$

(a diffusive estimate $\Phi_{\rm ED}$ is described below). Similarly, the surface heat flux can be evaluated from Φ_A just outside of the boundary layer:

$$Q_{0A} = \lim_{z\to 0;\, z<-\delta_s} \Phi_A(z)\rho C_p. \tag{20}$$

D'Asaro et al. (2002) show that both Q_{0A} and Q_{0L} equal Q_0 in a simulated mixed layer.

All three terms in (13) will be computed from the float data as well as Q_{0A}, Q_{0D}, Q_{EA}, and Q_{ED}. The consistency of these estimates will serve as a check on the accuracy of the measurements.

d. Heat flux—Lagrangian perspective

1) AVERAGING

The above derivation of Q_{0D} is problematic near the sea surface, particularly under hurricane conditions. The surface is not flat, so the upper limit of integration in (12) is not well defined, nor is the diffusive model of heat transport in (16) easy to apply to the frothy and wavy air–sea interface under high wind conditions. It is useful, therefore, to derive the results based on a purely Lagrangian view of the boundary layer that is free of these limitations.

Define a Lagrangian averaging operator $\{\ \}_X$, which takes a time average along the Lagrangian track for all times satisfying the condition specified by X. In addition, if multiple Lagrangian trajectories are available, $\{\ \}_X$ averages these together. If the statistics of the problem are sufficiently steady and/or there are enough trajectories then this Lagrangian average can be equated with a horizontal average

$$\{\ \}_{Z_1<z<Z_2} = \frac{1}{Z_2 - Z_1}\int_{Z_1}^{Z_2} \langle\ \rangle\, dz. \tag{21}$$

D'Asaro et al. (2002) and Harcourt et al. (2002) show that (21) is accurate for numerically simulated turbulent boundary layers.

The vertical advective heat flux Φ_A, and thus Q_{0A}, can be easily written using (21) as $\Phi_A(Z) = \{w\theta'\}_{z=Z}$.

2) LAGRANGIAN HEATING

Consider an ensemble of Lagrangian trajectories that uniformly sample the region $0 > z > -H$ so that (21) is true for floats in this region. Trajectories may also exit this region through the bottom boundary. Because the volume of the region is constant, the number of trajectories must be constant and each exiting trajectory must be replaced by an incoming trajectory. If, however, the identities of the outgoing and ingoing trajectories are switched so that the exiting trajectory ''bounces'' off the region bottom and assumes the properties of the incoming trajectory, then all trajectories can be made to stay within the region. These new trajectories may rapidly change their properties, such as temperature, at $z = -H$. This change can be considered to occur in a thin layer of thickness δ_e.

Divide the region into three layers: s for surface, e for entrainment, and i for interior. Surface heating occurs in layer s, $z > -\delta_s$. Exiting particles switch identity in layer e, $z > -H + \delta_e$. The remainder of the region is layer i. Let $\mathcal{P}(X)$ be the probability of trajectories being in layer X—that is, $\mathcal{P}(X) = t_X/T$, the time spent in layer X divided by the total time. Since the entire region is sampled uniformly

$$\mathcal{P}(s) = \frac{t_s}{T} = \frac{\delta_s}{H}, \tag{22}$$

$$\mathcal{P}(e) = \frac{t_e}{T} = \frac{\delta_e}{H}. \tag{23}$$

Assume that the region cools at an average rate $\overline{\Theta}_t$ driven by fluxes at the surface Q_0 and bottom Q_E, so that

$$\overline{\Theta}_t \rho C_p = \frac{Q_0}{H} - \frac{Q_E}{H}, \tag{24}$$

where Q_0 represents true heat input to the region, while Q_E represents exchange of particles with the underlying water. The total cooling must also equal the average rate of cooling of the Lagrangian trajectories:

$$\overline{\Theta}_t = \left\{\frac{D\theta}{Dt}\right\}_{\mathrm{all}}. \tag{25}$$

The Lagrangian heating can be divided by layer

$$\left\{\frac{D\theta}{Dt}\right\}_{\mathrm{all}} = \left\{\frac{D\theta}{Dt}\right\}_s \mathcal{P}(s) + \left\{\frac{D\theta}{Dt}\right\}_i \mathcal{P}(i) + \left\{\frac{D\theta}{Dt}\right\}_e \mathcal{P}(e). \tag{26}$$

The surface term represents the heating of the layer due to the surface flux,

$$Q_{OD} = \mathcal{P}(s) H \left\{\frac{D\theta}{Dt}\right\}_s \rho C_p, \tag{27}$$

which by (22) implies

$$Q_{0D} = \left\{\frac{D\theta}{Dt}\right\}_s \delta_s \rho C_p, \tag{28}$$

which is equivalent to (18).

If, as in the hurricane data, all mixed region trajectories return to the mixed layer, then Q_E can be computed by a variant of this method. Equation (26) is exactly true, since the total heating on each trajectory in each layer $\Delta\theta_X$ must sum to the overall total heating on that trajectory. Heating below H, the third term in (26), is assigned to Q_E:

$$Q_{\mathrm{ED}} = \rho C_p H \frac{\Delta\theta_e}{t_e}\mathcal{P}(e) = \rho C_p H \frac{\Delta\theta_e}{t_e}\frac{t_e}{T} = \rho C_p H \frac{\Delta\theta_e}{T} = \rho C_p H\left(\overline{\Theta}_t - \frac{\Delta\theta_{si}}{T}\right), \tag{29}$$

which has no Eulerian equivalent. The last two expressions show two different ways to compute Q_{ED}. Note that Q_{ED} as expressed above is not necessarily the same

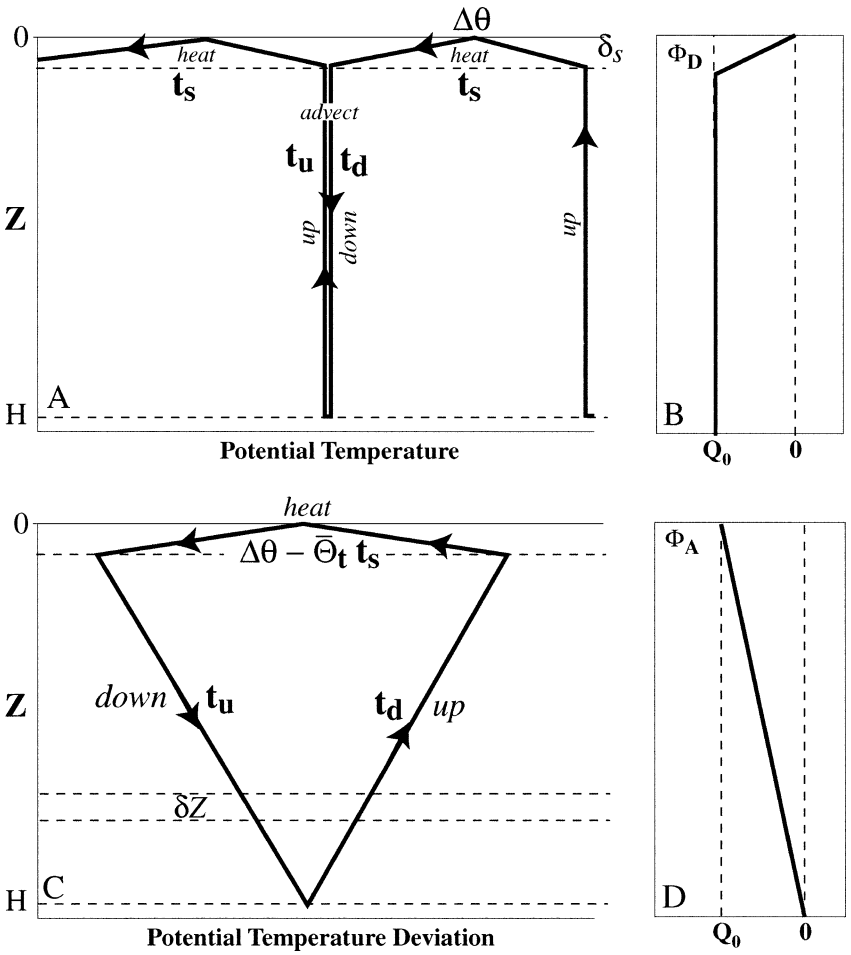

FIG. 5. (a) Idealized potential temperature/depth trajectory for Lagrangian paths in a layer cooled from above. (b) Profile of Φ_D for this trajectory. (c) Same trajectory but for deviation of potential temperature from layer mean. (d) Profile of Φ_A.

as $\rho C_p[\Phi_D(-\infty) - \Phi_D(-H)]$. Similar methods could be used to compute the surface flux. These would yield results that differ from (18) if $\mathcal{P}(z)$ is not uniform.

There are three important results of this analysis: First, the Lagrangian heating rate in the surface layer can be used to compute the surface heat flux. Second, the results are independent of the details of the Lagrangian path through the surface layer and the mechanism of heating; all that matters is the average time that is spent in the surface layer and the average change in temperature that occurs during this time. This is explicit in the variant (29). Third, these results require (22); the Lagrangian trajectory must spend equal amounts of time at each depth—that is, $\mathcal{P}(z)$ must be uniform for $z > -H$.

3) AN IDEALIZED PROBLEM

An idealized problem will help show the relationship between temperature changes along Lagrangian trajectories and heat fluxes. Again, consider a surface layer of depth H that is cooling under the influence of a heat flux Q_0 applied at the upper boundary (Fig. 5). This cools the entire layer at a rate $\overline{\Theta}_t = Q_0/H$. Lagrangian trajectories traverse the layer with depth $Z(t)$ and temperature $T(t)$. In the interior, there is no net heating or cooling so $dT/dt = 0$. All of the Lagrangian temperature change therefore occurs in the surface layer of thickness δ_s. The temperature changes by $\Delta\theta$ during each surface encounter. Trajectories require time t_d to traverse the layer going down—that is, from $Z = -\delta$ to $Z = -H$—and time t_u to traverse it going up. Trajectories take time t_s to traverse the surface layer, that is, from $Z = -\delta$ to $Z = 0$ to $Z = -\delta$. The trajectory must spend an equal time at all depths so

$$\frac{t_u}{H - \delta_s} + \frac{t_d}{H - \delta_s} = \frac{t_s}{\delta_s}. \tag{30}$$

The resulting trajectories $T(Z)$ are shown in Fig. 5a.

Because the layer is heated only at the surface,

$$\overline{\Theta}_t = \frac{Q_0}{H} = \frac{\Delta\Theta}{t_s + t_u + t_d} = \frac{\Delta\Theta}{t_s}\frac{t_s}{t_s + t_u + t_d}$$

$$= \left\{\frac{D\Theta}{Dt}\right\}_s \frac{\delta_s}{H} = \frac{Q_{0D}}{H}, \tag{31}$$

showing that $Q_{0D} = Q_0$. Here, $\Phi_D(z)$ rises from zero at the surface to Q_0 at $z = -\delta_s$ as shown in Fig. 5b.

The advective heat flux computed in a depth bin of width δZ at depth z is $\Phi_A(z) = \{w\theta'\}_{|z-\delta_z|<\delta Z/2}$. This average is the sum of contributions from the upgoing and downgoing legs of the trajectory each weighted by the time spent in the bin δt (see Fig. 5c):

$$\Phi_A = \frac{w_u\theta'_u\delta t_u + w_d\theta'_d\delta t_d}{\delta t_d + \delta t_u}, \tag{32}$$

where $w_u = (H - \delta_s)/t_u$ and $w_d = -(H - \delta_s)/t_d$ are the upward and downward velocities, respectively; θ'_u and θ'_d are θ' for the upward- and downward-going legs, respectively; and $\delta t_u = \Delta Z/w_u$ and $\delta t_d = \Delta Z/w_d$ are the times spent in the bin by the upward- and downward-going legs, respectively. Using these definitions,

$$\Phi_A = \frac{\theta'_d - \theta'_u}{\dfrac{1}{w_d} + \dfrac{1}{w_d}}. \tag{33}$$

The temperatures of the upward- and downward-going water parcels are the same (see Fig. 5a). Their perturbation temperatures θ' differ only because the mixed layer has changed temperature at a rate Θ_t in the time that it took for the trajectory to move between the two crossings of this bin (Fig. 5c). Substituting this time $(H + z)(w_u^{-1} + w_u^{-1})$ into (33) yields

$$\Phi_A = \Theta_t(H + z) = Q_0\frac{H + z}{H}. \tag{34}$$

The advective heat flux decreases linearly from Q_0 at the surface to 0 at $z = -H$ (Fig. 5d) as expected. Note from (33) that the advective heat flux depends only on the difference between the temperatures of the upward- and downward-going water parcels and the geometrical mean of their velocities.

Another simple Lagrangian interpretation results from writing the depth average advective heat flux as

$$\frac{1}{H}\int_{-H}^{0}\Phi_A(z)\,dz = \{\theta' w\}_{\text{all}} = \lim_{T\to\infty}\frac{1}{T}\int\theta' w\,dt$$

$$= \lim_{T\to\infty}\frac{1}{T}\oint\theta'\,dz. \tag{35}$$

The flux is the area enclosed by the $z - \theta'$ trajectory. Clockwise loops in $z - \theta'$ space imply a flux of cold water upward or warm water downward. This provides a useful qualitative diagnostic (D'Asaro et al. 2002) of the flux. For the simple problem in Fig. 5, δ and t_s are small and the area equals $H\Delta\Theta/2 = \overline{\Theta}_t/2$.

e. Computational issues

The measured float temperature and pressure often change significantly between samples (see Fig. 4). Estimates of $D\theta/Dt$ and w at a given time will therefore depend on how the data are interpolated and averaged. The values of Φ_D and σ_{wA} are particularly sensitive to these details.

A set of uniformly spaced depth bins of width δZ were defined. The values of potential temperature and pressure were assumed to vary linearly between data points, thus defining a continuous function of time for each. All derived quantities were computed using this function exactly; θ and P are continuous; $D\theta/Dt$ and w are discontinuous at data points and constant between them; vertical acceleration is a series of delta functions. The time average of these functions in computed in each bin remembering that a trajectory can pass through each bin many times. Note that with this scheme there is contribution to a given bin even if there are no data points in the bin.

There is only one free parameter δZ. Its value is limited by the approximate size of the float on the low end, since the float is not Lagrangian on scales smaller than this, and by the size of the variation of the functions of interest on the high end. The calculations use 1 m and are not sensitive to the choice.

f. Dissipation rates and diapycnal fluxes

Lien et al. (1998), D'Asaro and Lien (2000), and Lien et al. (2002) use spectra of Lagrangian acceleration $\Phi_{ww}(\omega)$ to estimate the rate of turbulent kinetic energy dissipation ε. Measurements of $\Phi_{ww}(\omega)$ using Lagrangian floats in a variety of both stratified and unstratified environments show a clear pattern of spectral shapes. At Lagrangian frequencies ω above a large-eddy frequency ω_0, and below a frequency $\omega_L = (\varepsilon/L^2)^{1/3}$ set by the float size L, there is a turbulent inertial subrange in which $\Phi_{ww}(\omega)$ is white with a spectral level $\beta\varepsilon$, where β is a Kolmogorov constant with a value of 1.7–2.2 (Lien and D'Asaro 2002). We use 1.8. In the stratified thermocline ω_0 is about $0.5N$. The diapycnal eddy diffusivity can be computed following Osborn (1980), and a host of others:

$$K_O = 0.2\frac{\varepsilon}{N^2}. \tag{36}$$

Lien et al. (2002) suggest that the rate of temperature variance dissipation χ can be computed in a similar manner. In the inertial subrange, the Lagrangian frequency spectrum of $D\theta/Dt$, $\Phi_{\dot\theta\dot\theta}(\omega)$ is white with a spectral level $\beta_T\chi$, where β_T is a Kolmogorov constant with a value of about $1/\pi$. In the stratified thermocline the diapycnal eddy diffusivity can be computed following Osborn and Cox (1972) and Winters and D'Asaro (1996):

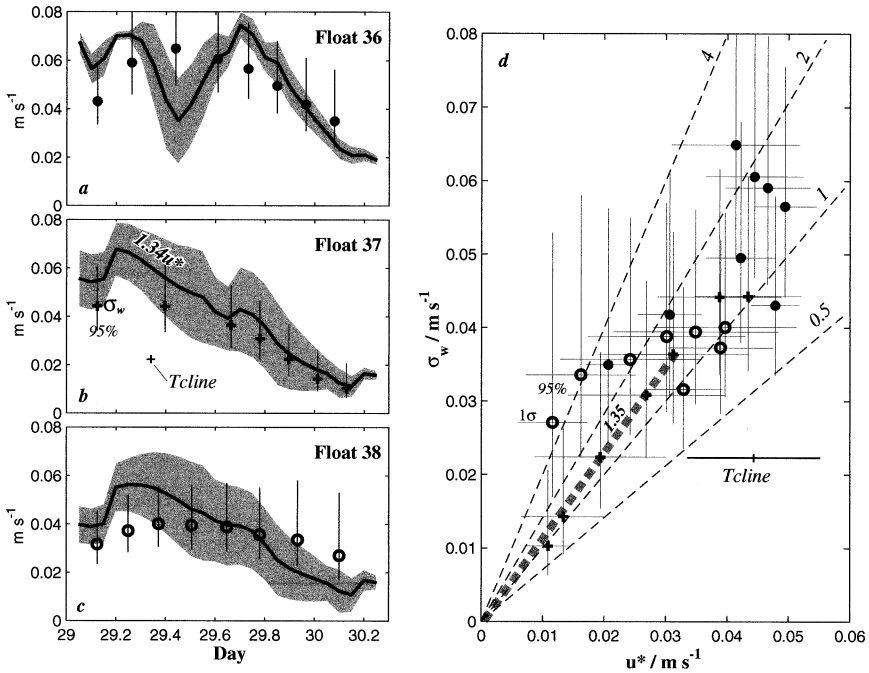

FIG. 6. (a)–(c) Time series of 20 000-s-averaged, half-overlapped rms vertical velocity σ_w (symbols) in the mixed layer (above $H = 40$ m) with 95% χ^2 confidence limits (vertical lines) and scaled friction velocity $\sqrt{1.8}u_*$ with one std dev (filled) (the std dev of u_* is the same as in Fig. 2). (d) Scatterplot of u_* with σ_w for all three floats. Error bars as in (a)–(c). Each float uses a different symbol, as shown in (a)–(c). Dashed lines show ratio of u^2 to σ_w^2 as labeled. The shorter, thicker dashed line shows the ratio and range of u_* found by D'Asaro (2001). The data point labeled ''Tcline'' is a data point from below the mixed layer (float 37); no error bars for σ_w are shown. For data in the mixed layer, degrees of freedom for σ_w were computed as $T_{av}/T_c \langle 1/\tau \rangle \tau$, where $T_{av} = 20\,000$ s is the averaging time, $T_c = 750$ s is the estimated correlation time of vertical velocity, and $\tau = u_*/H$ and $1/\langle 1/\tau \rangle = 1100$ s is its typical value.

$$K_{OC} = \frac{\chi}{2\overline{\Theta}_z^2}, \tag{37}$$

where $\overline{\Theta}_z$ is an average vertical gradient of potential temperature. Several different ways of computing $\overline{\Theta}_z$ have been suggested (Winters and D'Asaro 1996), which result in different interpretations of K_{OC}. Practically, the differences are probably small (D'Asaro et al. 2002).

Heat flux will be computed using both (36) and (37). These results will be compared with other methods and will act as another check on the accuracy of the data and analysis methods.

5. Results

a. Energetics

1) VERTICAL KINETIC ENERGY

Figure 6 compares the rms vertical velocity σ_w from float data in the mixed layer with the estimated friction velocity u_*. D'Asaro (2001) finds a strong correlation between these with $\sigma_w^2 = \overline{A}u_*^2$ and a best-fit value of $\overline{A} = 1.35 \pm 0.07$. The hurricane data (Fig. 6d) show a similar relationship, but with a large scatter. Time series plots for the individual floats in Figs. 6a–c show only a weak relationship between u_* and σ_w. Note that the value of $\overline{A}$ appears smaller at the start of the storm than near the end and that the decrease in wind stress as float 36 passed close to the eye is not reflected in σ_w. Given the large errors in u_* caused by the uncertainty in float position, it is unwise to draw more detailed conclusions.

Figures 7a, 8a, and 9a show the average profile of $\sigma_w^2(z)$ for each float, the profile of $\sigma_{wA}^2(z)$ computed using (7), and the probability distribution of float depth $\mathcal{P}(z)$. All three floats show a near-surface maximum in vertical kinetic energy.

The probability distribution is largest near the surface and decreases with depth for all three floats. Kinematically, this is consistent with an increasing deviation of σ_{wA}^2 from σ_w^2—that is, an anomalous tendency for floats starting at the surface to turn upward with depth, while their water parcels continue downward. Dynamically, there are two possible explanations. First, the floats may be buoyant, which is consistent with the fact that they all float to the surface after the hurricane passes. Harcourt et al. (2002) and D'Asaro et al. (2002) show ex-

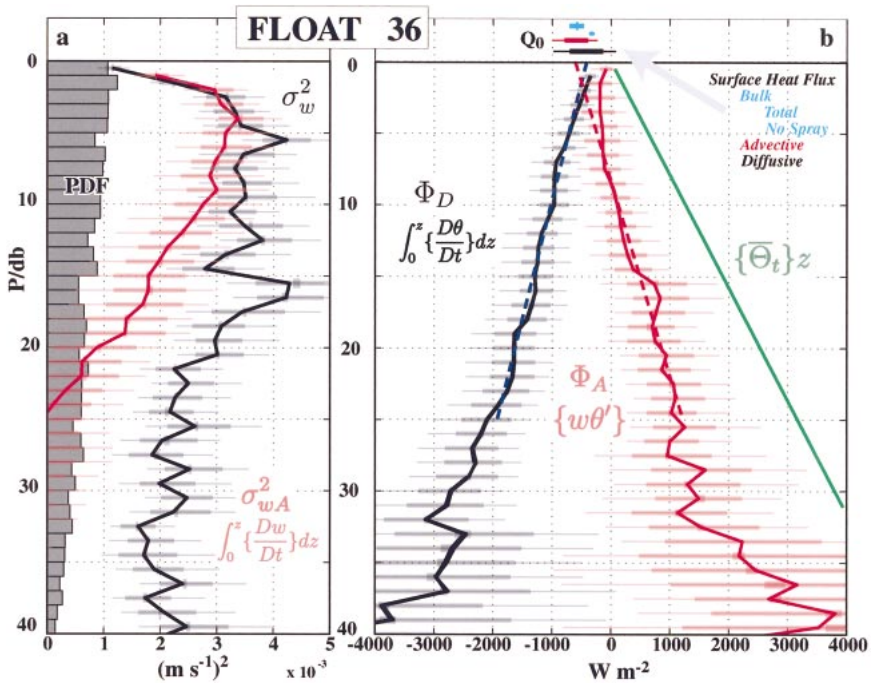

FIG. 7. (a) Profile (black) of vertical variance σ_w^2 from float 36 on 29 Aug. Profile (red) of σ_{wA}^2 computed from vertical acceleration using (6). Probability distribution of float pressure plotted as bar plot. (b) Profiles of terms in (13) as labeled. Surface heat flux computed from advective Q_{0A} (20) and diffusive Q_{0L} (18) terms are plotted at negative pressures for ease of viewing. These are computed from linear fits over 5–25 dbar to the appropriate curve and extrapolating to the surface. Bulk fluxes from Fig. 2 are also shown. Error bars for all quantities are 0.03%, 0.5%, and 0.95% points computed from the distribution of 300 resamplings of the data in each bin, i.e., bootstrapping (Efron and Gong 1983).

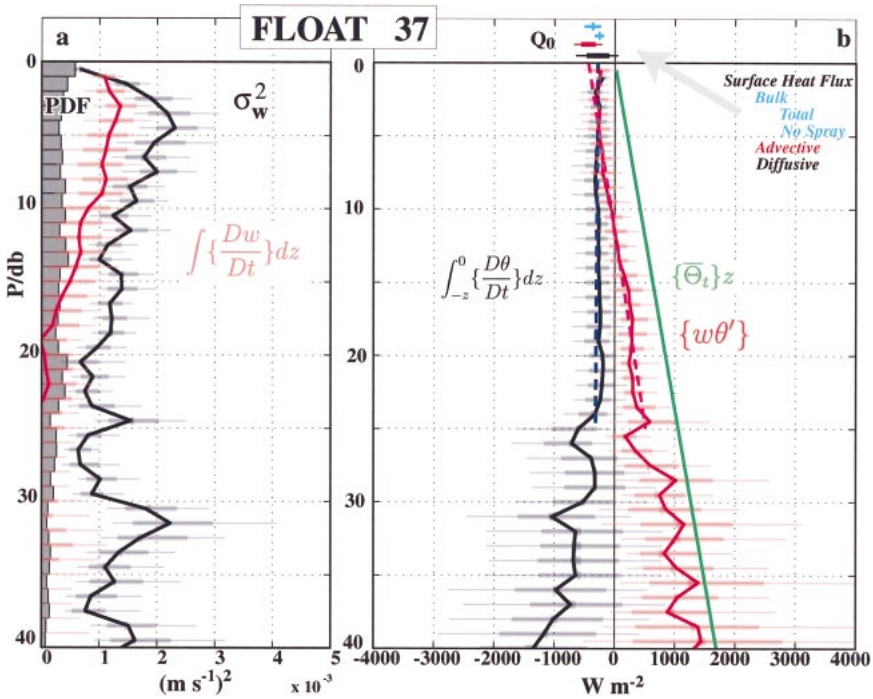

FIG. 8. Same as Fig. 7, but for float 37.

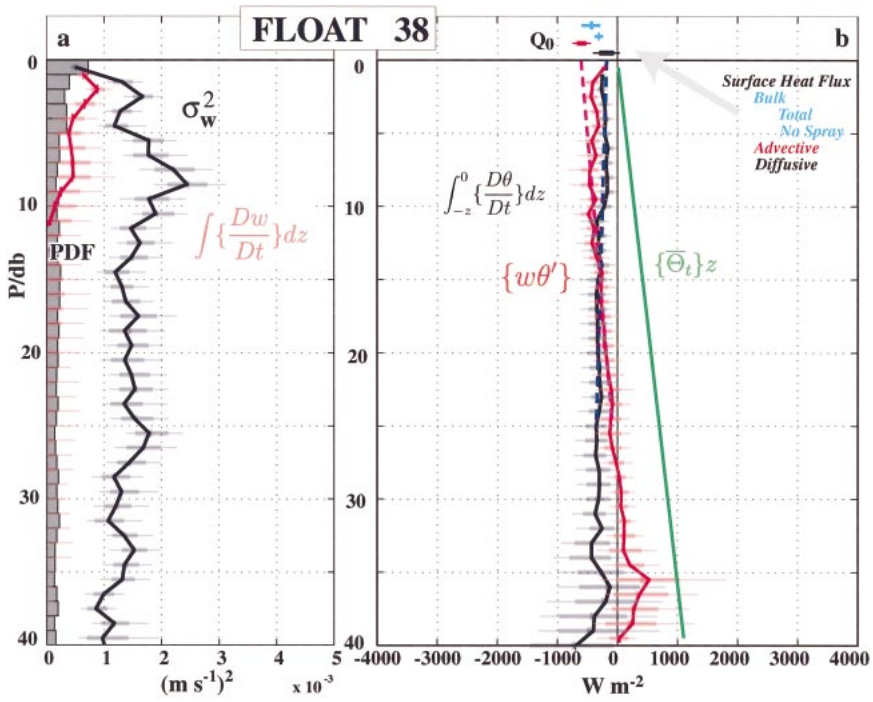

FIG. 9. Same as Fig. 7, but for float 38.

amples of this behavior. Alternatively, the floats may be confined to a mixing layer whose depth varies rapidly with time because of the strong vertical or horizonal entrainment of heavier water. Floats spend more time at shallow depths because the mixed layer is more often shallow than deep. D'Asaro (2001) shows a wind-driven boundary layer with these properties.

By these measures, float 36 appears to be the most Lagrangian and float 38 the least Lagrangian. Although the relationship between these statistics of float error and the ability of the floats to measure other Lagrangian statistics is not well understood, similar unpublished calculations made using the data described in D'Asaro (2001) indicate that floats 36 and 37 are sufficiently Lagrangian to make accurate heat flux measurements.

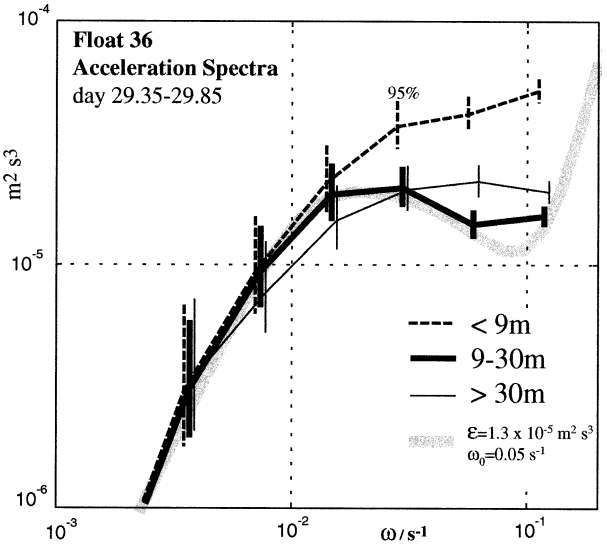

FIG. 10. Spectra of vertical acceleration from float 36 during the period of strongest winds, day 29.35–29.85. Spectra are computed from wavelet coefficients averaged into depth bins as indicated by the legend. Error bars show 95% confidence limits of a χ^2 distribution. Thick shaded line shows spectral form computed by Lien et al. (1998) for kinetic energy dissipation rate $\varepsilon = 1.3 \times 10^{-5}$ m^2 s^{-3}, large-eddy frequency $\omega_0 = 0.05$ s^{-1}, a float half-height of 0.5 m, and a pressure bit noise of 8 cm.

2) KINETIC ENERGY DISSIPATION

Figure 10 shows spectra of vertical acceleration for float 36 in three depth ranges. These were computed using a maximum-overlap wavelet method (Percival and Guttorp 1994) of the lowest order difference estimate of acceleration, which yields spectral estimates with periods of 40, 80, 160 . . . s every 20 s. The individual estimates were then averaged in depth bins to form spectra. The spectra were corrected for the response function of the differencing, although the correction is imperfect for the highest frequency wavelet. Note that the frequency at which the float moves through the mixed layer is about 0.01 s^{-1}. At frequencies comparable to or less than this the energy in a given wavelet is spread out over the entire boundary layer and all depth bins have the same spectral level.

As described in section 4f, the rate of dissipation of turbulent kinetic energy ε is given by the level of the

acceleration spectrum within the inertial subrange of frequencies. The thick gray line in Fig. 10 shows the spectral form of Lien et al. (1998) fit to the 9–30-m spectrum using $\varepsilon = 1.3 \times 10^{-5}\ \mathrm{m^2\ s^{-3}}$. Assuming isotropy and a vertical kinetic energy of about $(0.06\ \mathrm{m\ s^{-1}})^2$ in the mixed layer, the dissipation time $1.5\sigma_w^2/\varepsilon$ is about 415 s, during which the rms velocity can move a water parcel 25 m, about the depth of the mixed layer.

Near the surface the acceleration spectra are larger and bluer, presumably reflecting both a larger dissipation rate and a smaller eddy size. Our universal spectra are not appropriate in this case. At deeper levels, the spectral levels are also high and somewhat blue, reflecting high dissipation levels but smaller eddy scales due to stratification.

b. Heat fluxes

1) ANALYSES

Figures 7b, 8b, and 9b show the vertical integrals of the three terms in the upper ocean heat budget (13) for float 36 (east), 37 (west), and 38, respectively. All were computed using a consistent interpolation and binning scheme, as described in section 4e. Each pass of the float through each bin produced one number that contributed to the averages of quantities in that bin. Confidence limits were computed by randomly resampling these numbers to form 300 realizations of all computed quantities. Confidence limits were computed from the distribution of these realizations for each quantity. The 70% confidence limits were used to approximate the standard deviation of the various fluxes listed in Table 1. No confidence limits were computed for Q_{ED} as it is difficult to generate independent realizations of (29) subject to the constraint of (26).

The Eulerian heating term $\overline{\Theta}_t$ was evaluated from a least squares linear fit to all potential temperature measurements shallower than $H = 30$ m for day 29. Potential temperature is assumed uniform with depth so the integral of the Eulerian heating term $\overline{\Theta}_t z$ is linear with depth. The negative of this is plotted as a green line, multiplied by ρC_p to cast it into units of W m^{-2}.

The vertical advective heat flux $\Phi_A = \{w\theta'\}(z)$ was computed using a high-pass filter of the potential temperature θ. First, $\overline{\Theta}(t)$ was computed as a fourth-order polynomial fit to all temperatures shallower than 30 m. Then $\theta'' = \theta - \overline{\Theta}$ was computed. This was high-pass filtered using a sine filter of length $T_{\mathrm{hp}} = 5000$ s to compute θ'. Smaller values of T_{hp} produced smaller values of Φ_A while larger values resulted in larger errors with little change in the mean.

Normally we expect $\Phi_A(z)$ to vary linearly with depth within a mixed layer so that its depth derivative is uniform with depth and it uniformly heats the mixed layer. Deviations from linearity occur near the surface and at the mixed layer base, where diffusive and/or radiative fluxes are nonzero. The profiles of $\Phi_A(z)$ are nearly linear in the center of the mixed layers and were therefore fit with a least squares line from 5 to 25 m. The slope of the line gives the net heating of the mixed layer; its flux extrapolated to the surface gives the surface heat flux Q_{0A} (20); its flux extrapolated to 30 m gives the entrainment heat flux Q_{EA} (19).

The diffusive heat flux $\Phi_D(z)$ is expected to be constant except in a thin surface layer and in the entrainment zone (D'Asaro et al. 2002). The profiles are also fit with a least squares line from 5 to 25 m. The slope of the line is the net heating of the mixed layer due to this term; its value extrapolated to the surface gives the surface heat flux Q_{0D} (18). The total heating below H is used to compute Q_{ED} (29).

2) THE MIXED LAYER HEAT BUDGETS

(i) Accuracy

The top section of Table 1 lists the terms in the mixed layer heat budget for each float. The budgets close with accuracies far less than the error bars; that is, the ''residual'' in line 4 of Table 1 is small. This may be a result of the self-consistent manner in which the quantities were computed. If so, the residual is not necessarily a measure of the accuracy of the methods.

The difference between the advective and diffusive estimates of the surface heat flux may be a better estimate of the errors. For floats 36 and 37, this difference was 20%–40%, comparable to the statistical uncertainty in the estimates. For float 38, the differences are much larger. This, combined with the large difference between σ_w^2 and σ_{wA}^2 for float 38 and the surface peak in the float depth distribution indicates that float 38 was buoyant and that this buoyancy led to sufficient non-Lagrangian behavior to make the flux measurements inaccurate.

Comparison between the surface heat fluxes estimated from the floats and from bulk formulas are difficult due to the large errors in both quantities. However, for both float 36 and 37, the average of Q_{0A} and Q_{0L} deviated by only about 5% from the corresponding bulk heat flux estimate. For both, the ''no spray'' estimate was less than either Q_{0A} or Q_{0L}. This is consistent with the hypothesis that spray significantly increases the air–sea heat flux during hurricanes.

(ii) Why does SST cool?

Clear differences between the heat budgets at the three floats emerge from these data. Float 37, on the left-hand (west) side of the storm, exhibited the classic entraining boundary layer profile. Here, Φ_A was linear with an entrainment heat flux of about three times the surface heat flux, and Φ_D increased rapidly near the surface, but was constant in the mixed layer interior. Thus in the layer interior, there was a clear balance between heating and vertical advection.

The flux pattern for float 38 was similar to that of

TABLE 1. Heat budgets of the upper ocean, day 29–30. All numbers are in units of watts per square meter although written as temperature fluxes. Error ranges (in parentheses) are ± one std dev from mean.

Float	36	37	38
0–30-m heating rate			
(a) $\overline{\Theta}_t H$	−3802 (−3770 −3832)	−1286 (−1256 −1316)	−838 (−808 −868)
(b) $\Phi_A\|^0_{-30}$; 5–25-m fit	−2196 (−1761 −2631)	−1144 (−868 −1424)	−628 (−468 −788)
(c) $\Phi_D\|^0_{-30}$; 5–25-m fit	−1821 (−1208 −2444)	−47 (−276 361)	−205 (45 −455)
Residual (a) − (b) + (c)	215 (−536 966)	−95 (323 −513)	−5 (302 −292)
Surface heat flux			
$\Phi_A(0)$; 5–25-m fit	−605 (−406 −804)	−436 (−317 −555)	−602 (−523 −681)
$\Phi_D(0)$; 5–25-m fit	−413 (−133 −693)	−278 (−96 −460)	−181 (−61 −301)
Difference/mean	37%	44%	107%
Bulk formulas	−583 (−462 −704)	−371 (−233 −509)	−440 (−285 −595)
Bulk formula, no spray	−328 (−283 −373)	−258 (−181 −335)	−308 (−240 −376)
Entrainment heat flux			
$\Phi_A(-30\text{m})$; 5–25-m fit	1571 (1326 1816)	695 (541 849)	16 (97 −65)
Q_{ED}	1502	852	−184
Difference	69	−157	−168
ϵ using (36)	5070 (3550 6590)	442 (315 618)	
χ using (37)	6325 (3680 9660)	1717 (1073 2504)	

float 36. This is to be regarded with caution because the float was poorly ballasted.

Float 36, on the right-hand (east) side of the storm, exhibited the largest cooling, equivalent to nearly 4000 W m^{-2} heat flux divergence. This was not due to the surface cooling, but to large entrainment (1600 W m^{-2}) and Lagrangian heating (1800 W m^{-2}) terms. The entrainment is easy to understand; strong inertial currents on this side of the storm led to strong entrainment. The Lagrangian heating, however, implies a heat source distributed throughout the mixed layer. A satellite SST image (Fig. 11) taken just after Dennis's passage suggests a possible source for this cooling. A strong east–west temperature gradient is apparent; the warmest waters were in the Gulf Stream, near float 38. A band of water about 2.5°C cooler extended 200 km eastward from Dennis's track. This was probably due both to cooling on the east side of the storm and to preexisting gradients. A broad front, corresponding roughly with Dennis's track, marked the western boundary of this colder water. Float 36 was deployed west of this front, on the warm side, and surfaced east of it, in the colder water. The SST image suggests that a cyclonic eddy on the front advected the warm water containing float 36 into the colder region. In the Lagrangian frame following float 36, this would appear as a horizontal heat flux divergence as the warm water is stirred into its colder surroundings. Water moving into the region and the cooling from E to F in Fig. 4 show an example of this cooling; the net Lagrangian cooling from 0 to 30 m at float 36 is explained as the sum of such events. Thus, the strong cooling at float 36 was primarily due to mixing with underlying cold water (entrainment) and mixing with surrounding cold water (horizontal mixing) with a small contribution from heat loss to the atmosphere.

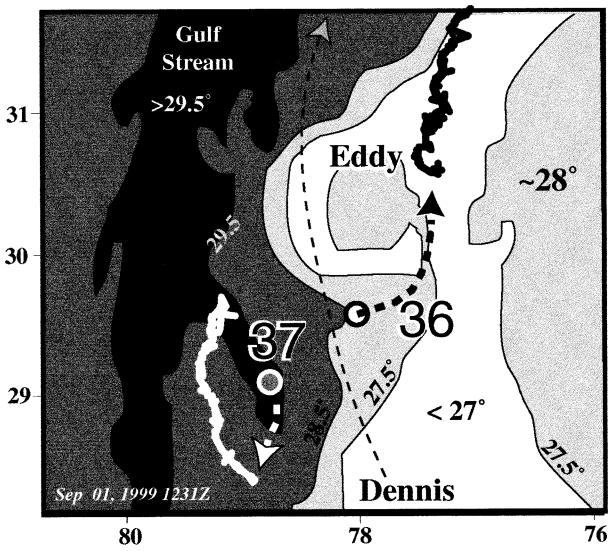

FIG. 11. Sketch of a satellite SST image on 1231 UTC 1 Sep, 3 days after Dennis's passage. The thin dashed line indicates the track of the hurricane. Launch positions (circles) of floats, positions after surfacing (heavy lines), and interpolated tracks (dashed) are shown. Interpolated tracks are guided by mesoscale features evident in the image. SST before the hurricane was 29°–31°C.

3) MICROSTRUCTURE HEAT FLUXES

Heat fluxes were computed during the short periods when floats 36 and 37 were in the thermocline using (36) and (37) as described in section 4f. Although these fluxes are not averaged over the same period as the other fluxes, they serve as a useful comparison.

Figure 12a shows the profile of perturbation temperature for float 36; the deepest excursion occurred near day 29.5; the flux was computed for this period. The vertical temperature gradient was 0.04–0.07°C m^{-1}; ignoring salinity, this corresponds to a vertical stratifi-

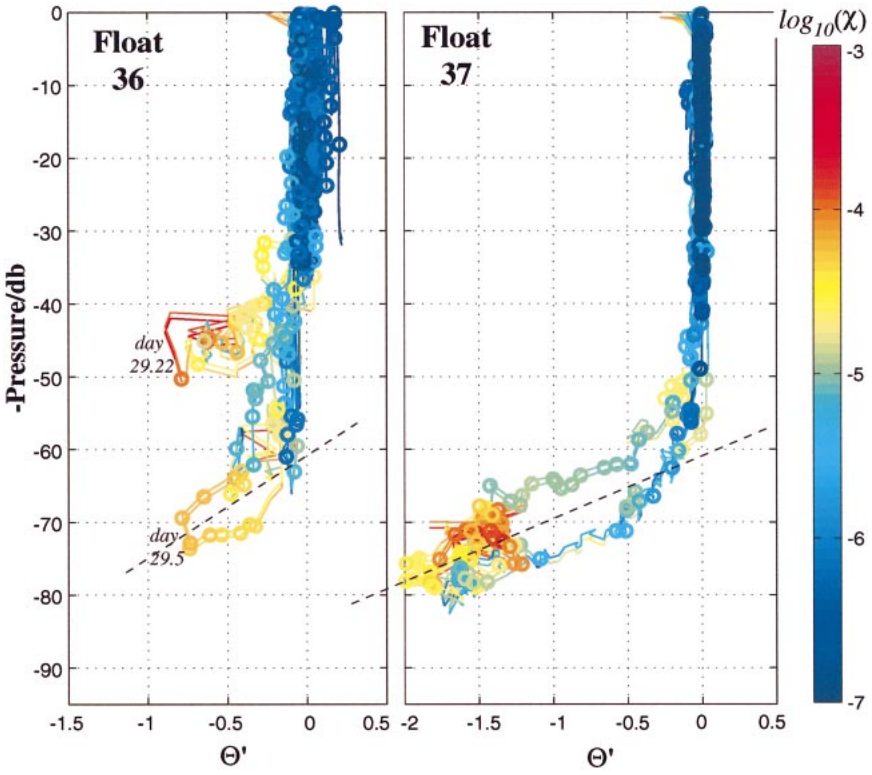

FIG. 12. Profiles of perturbation temperature θ' for floats 36 and 37. Lines are colored according to spectral level of $D\theta/Dt$ in wavelets with 80- and 160-s periods averaged over 100 s. Colored circles are drawn if ratio of spectral energy in the two wavelets is between 0.7 and 1/0.7, i.e., if the spectrum is approximately white. Thin dashed lines show approximate temperature gradients used to compute diapycnal fluxes.

cation $N = 0.011$–$0.015\ \mathrm{s}^{-1}$. D'Asaro and Lien (2000) find that the inertial subrange in a turbulent stratified fluid begins at a frequency of about N, which includes the highest three wavelet frequencies. Using the mean of the second and third (40- and 160-s periods), for times when the float is deeper than 30 m, $\varepsilon = 1.6 - 2.2 \times 10^{-5}\ \mathrm{m}^2\ \mathrm{s}^{-3}$, $K_O = 0.014 - 0.036\ \mathrm{m\ s}^{-2}$, and the heat flux is 3550–6590 W m^{-2}.

The coloring in Fig. 12a shows the spectral density of $D\theta/Dt$ for the second and third wavelets. The level is low in the mixed layer and high in the underlying stratification, as would be expected for χ, the rate of dissipation of temperature variance. If the spectral level of the two wavelets differ by less than 30%, the spectrum is judged to be sufficiently white to estimate χ and a circle is drawn. During the first thermocline excursion of float 36 (day 29.22), the spectra were not sufficiently white; during the second (day 29.5) they were. This yields a value of $\chi = 1.3$–$1.9 \times 10^{-4}\ \mathrm{C}^2\ \mathrm{s}^{-1}$, and, using (37), $K_{\mathrm{OC}} = 0.013$–$0.06\ \mathrm{m}^2\ \mathrm{s}^{-1}$, and a heat flux of 3680–6440 W m^{-2}. The heat fluxes derived from χ and ε agree to within their rather large computational errors.

Similar estimates for float 37 (see Table 1) yield much smaller entrainment heat fluxes, consistent with both the mixed layer measurements and the expected smaller inertial currents and shears on the left-hand side of the storm. In this case, the heat fluxes from χ are significantly larger than those from ε.

c. Other features

1) THE SURFACE LAYER

Heat is transferred from the atmosphere to the water within the surface layer. Here, Φ_A is not linear and Φ_D increases rapidly. Figures 7b, 8b, and 9b suggest that this layer was about 5 m thick, comparable to that found in the Labrador Sea by Steffen and D'Asaro (2002). The near-surface small clockwise loops in Fig. 4 suggest the presence of small heat-carrying eddies within this layer.

Within the top 2 m, a cool water layer was evident (Fig. 12). The shallowest temperature measurement was often 0.1°C colder than the nearby measurements, indicating the presence of a thin surface layer cooled directly by the atmosphere. Presumably this water is entrained into cold, downward-going plumes that carry the advective heat flux (Gemmrich and Farmer 1999).

2) SKEWNESS, FLUXES, AND ENTRAINMENT

The vertical velocity within the boundary layer has a clear asymmetry, with stronger velocity downward

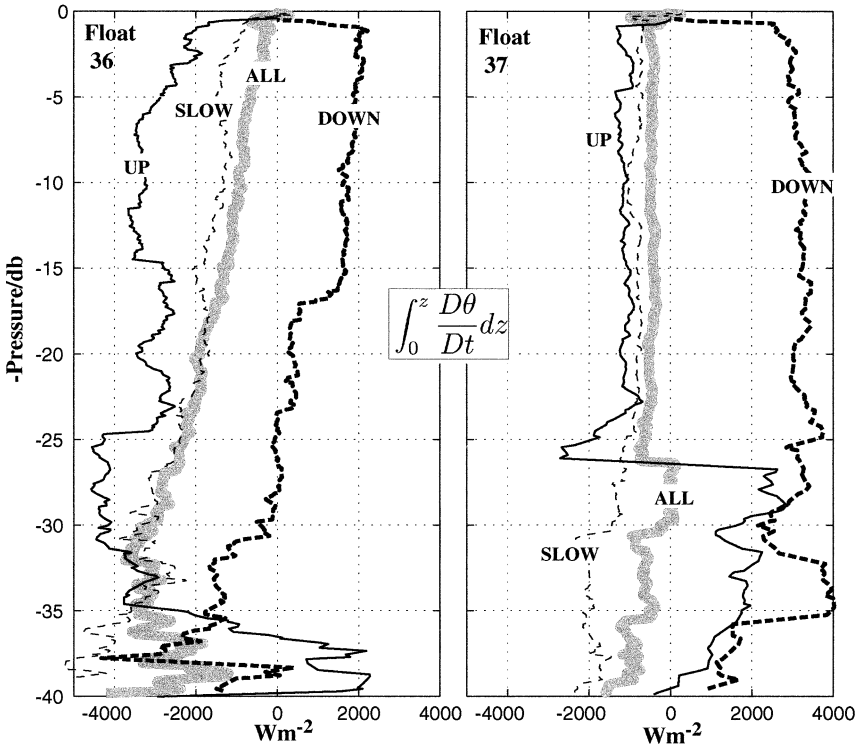

FIG. 13. Integrated Lagrangian heating for up ($w > 0.03$ m s^{-1}), down ($w < -0.03$ m s^{-1}), slow ($|w| < 0.03$ m s^{-1}), and all data.

than upward. This is measured by the skewness $\langle w^3 \rangle / \sigma_w^3$, which for day 29 was about 0.5 at middepth in the boundary layer and rose to about 1 near the surface. Alternatively, the average upward speed was 0.045 m s^{-1}, while the average downward speed was 0.052 m s^{-1}. (Speeds less than 0.01 m s^{-1} were excluded from both of these averages.) The maximum downward speed was 0.22 m s^{-1}, substantially larger than the maximum upward speed of 0.017 m s^{-1}.

Water exiting the surface layer undoubtedly carried properties of the surface layer into the interior. Many of these, such as bubbles and dissolved gas, could not be measured by the DLF. However, the surface layer was also a source of small-scale turbulent kinetic energy and this is clearly carried downward into the layer interior. The energy in wavelet 2 (40-s period) was typically 3–10 times larger when a float was travelling downward than when it was going upward.

Figure 13 shows the distribution of Lagrangian heating between upgoing, downgoing and slow vertical velocities for floats 36 and 37. Individual w estimates were sorted by depth and depth-integrated with no binning. This is simple and yields high depth accuracy, but is less accurate, especially near the surface, than the methods described in section 4e. Float 37 yielded no surprises; all the heating occurred near the surface; below 25 m the data were noisy. Float 36, however, showed that the interior heating occurred primarily when the float was going down; much less heating occurred when the float was rising or was slow. Perhaps this was because the downgoing water had more small-scale energy and thus could more easily mix the cold water that was intruding into its path from the side.

6. Summary and discussion

Three neutrally buoyant floats were air-deployed ahead of Hurricane Dennis in late August 1999. These floats were designed to accurately follow three-dimensional water trajectories. The floats measured pressure, that is, their own depth, and temperature. All three floats functioned, but one, deployed in the warm waters of the Gulf Stream, was excessively buoyant, which significantly biased the results. The hurricane passed between the other two floats, so that both measured the properties of the oceanic boundary layer beneath sustained winds of about 30 m s^{-1}, but on opposite sides of the storm. Major results include the following.

- Boundary layer and sea surface temperature cooled about 2.8° and 0.75°C at the floats on the east and west sides of the northward-going storm, respectively. Significant cooling (45% and 75%) occurred before the passage of the eye suggesting that such cooling can play an important role in hurricane thermodynamics (Emanuel 1999).
- The floats repeatedly moved through a mixed layer 30–70 m deep at average speeds of 0.03–0.06 m s^{-1}.

This speed was approximately proportional to the friction velocity u_* computed from operational hurricane wind products using the Large and Pond (1981) neutral drag coefficient. The proportionality constant was close to that found by D'Asaro (2001) in the wintertime North Pacific.

- All three terms in the horizontally averaged heat equation were computed from the float data yielding consistant estimates of the surface heat flux and entrainment heat fluxes from the advective and diffusive terms. Heat fluxes in the ocean boundary layer were several thousand watts per square meter. With only a single float at each location, however, the errors were also large, typically 30%.
- The surface heat fluxes computed from float measurements were larger than those computed from standard bulk formulas unless the effect of spray was included. The errors in both estimates, however, are sufficiently large to prevent a definitive conclusion on the importance of spray fluxes.
- Surface heat fluxes were smaller than entrainment heat fluxes, accounting for only 13% and 27% of the total boundary layer heating on the east and west sides of the storm, respectively. Mixing of cold water into the boundary layer was more important than loss of heat to the atmosphere. Most of the thermal energy available to power this hurricane was therefore extinguished by entrainment.
- Much more cooling occurred on the east than on the west side of the storm, presumably because of the much larger inertial currents and thus shear mixing on the right-hand (east) side. This was reflected in the larger entrainment heat flux on the eastern side (1600 W m^{-2}) as opposed to on the western side (800 W m^{-2}).
- About one-half of the cooling at the eastern float was due to advection of this float into colder water. This appears, on average, as a cooling distributed uniformly across the mixed layer, but resulted from individual cooling events concentrated at times when the float was vertically stationary or descending.
- The mixed layer turbulence was asymmetric with slightly faster downward speeds than upward speeds and much higher small-scale turbulence levels in downward going parcels.

The various Lagrangian consistency tests clearly show that these floats are only imperfectly Lagrangian. Despite this, floats 36 and 37 appear to give good heat fluxes within large statistical errors. Clearly, there is a need to understand the biases in these measurements due to float buoyancy and other errors, and to develop a better understanding of how the consistency tests can be used to assess the accuracy of computed heat fluxes. However, the floats appear capable of making useful measurements in these severe environments where other measurement techniques are difficult. More accurate heat flux measurements will require the deployment of float clusters to reduce the statistical noise, as done successfully in the Labrador Sea (Steffen and D'Asaro 2002).

Acknowledgments. This work was supported by NSF Grant OCE 9816807 and ONR Grant N00014-00-1-0893. The assistance of Peter Black in providing guidance into the world of hurricanes is gratefully acknowledged. Michael Ohmart built the floats and air-deployment system; without his cheerful and thorough work nothing would have happened.

REFERENCES

Andreas, E. L, 1998: A new sea spray generation function for wind speeds up to 32 m s^{-1}. *J. Phys. Oceanogr.,* **28,** 2175–2184.

Cione, J. J., P. G. Black, and S. H. Houston, 2000: Surface observations in the hurricane environment. *Mon. Wea. Rev.,* **128,** 1550–1561.

D'Asaro, E., 1985: The energy flux from the wind to near-inertial motions in the surface mixed layer. *J. Phys. Oceanogr.,* **15,** 1043–1059.

——, 2001: Turbulence intensity in the ocean mixed layer. *J. Phys. Oceanogr.,* **31,** 3530–3537.

——, 2003: Performance of autonomous Lagrangian floats. *J. Atmos. Oceanic Technol.,* in press.

——, and R. C. Lien, 2000: Lagrangian measurements of waves and turbulence in stratified flows. *J. Phys. Oceanogr.,* **30,** 641–655.

——, D. M. Farmer, J. T. Osse, and G. T. Dairiki, 1996: A Lagrangian float. *J. Atmos. Oceanic Technol.,* **13,** 1230–1246.

——, K. B. Winters, and R. C. Lien, 2002: Lagrangian analysis of a convective mixed layer. *J. Geophys. Res.,* **107** (C5), 3040, doi: 10.1029/2000JC000247.

Dickey, T., and Coauthors, 1998: Upper-ocean temperature response to Hurricane Felix as measured by the Bermuda testbed mooring. *Mon. Wea. Rev.,* **126,** 1195–1201.

Efron, B., and G. Gong, 1983: A leisurely look at the bootstrap, the jackknife and cross-validation. *Amer. Stat.,* **37,** 36–48.

Emanuel, K. A., 1999: Thermodynamic control of hurricane intensity. *Nature,* **401,** 665–669.

Gemmrich, J. R., and D. M. Farmer, 1999: Near-surface turbulence and thermal structure in a wind-driven sea. *J. Phys. Oceanogr.,* **29,** 480–499.

Harcourt, R. R., E. L. Steffen, R. W. Garwood, and E. A. D'Asaro, 2002: Fully Lagrangian floats in Labrador Sea deep convection: Comparison of numerical and experimental results. *J. Phys. Oceanogr.,* **32,** 493–510.

Jacob, S. D., L. K. Shay, A. J. Mariano, and P. G. Black, 2000: The 3D mixed layer response to Hurricane Gilbert. *J. Phys. Oceanogr.,* **30,** 1407–1429.

Large, W., and S. Pond, 1981: Open ocean momentum flux measurements in moderate to strong wind. *J. Phys. Oceanogr.,* **11,** 324–336.

Lawrence, M. B., L. A. Avila, J. L. Beven, J. L. Franklin, J. L. Guiney, and R. J. Pasch, 2001: Atlantic hurricane season of 1999. *Mon. Wea. Rev.,* **129,** 3057–3084.

Lien, R. C., and E. A. D'Asaro, 2002: The Kolmogorov constant for the Lagrangian velocity spectrum and structure function. *Phys. Fluids,* **14,** 4456–4459.

——, ——, and G. T. Dairiki, 1998: Lagrangian frequency spectra of vertical velocity and vorticity in high-Reynolds number oceanic turbulence. *J. Fluid Mech.,* **362,** 177–198.

——, ——, and M. J. McPhaden, 2002: Internal waves and turbulence in the upper central equatorial Pacific: Lagrangian and Eulerian observations. *J. Phys. Oceanogr.,* **32,** 2619–2639.

Osborn, T. R., 1980: Estimates of the local rate of vertical diffusion from dissipation measurements. *J. Phys. Oceanogr.,* **10,** 83–89.

——, and C. S. Cox, 1972: Oceanic fine structure. *Geophys. Fluid Dyn.,* **3,** 321–345.

Percival, D. B., and P. Guttorp, 1994: Long-memory processes, the Allan variance and wavelets. *Wavelets in Geophysics,* E. Foufoula-Georgiou and P. Kumar, Eds., Academic Press, 325–343.

Pollard, R. T., and R. C. Millard, 1970: Comparison between observed and simulated wind-generated inertial oscillations. *Deep-Sea Res.,* **17,** 153–175.

Powell, M. D., S. H. Houston, L. R. Amat, and N. Morisseau-Leroy, 1998: The hrd real-time hurricane wind analysis system. *Eng. Ind. Aerodyn.,* **77–78,** 53–64.

Price, J., T. Sanford, and G. Forristall, 1994: Forced stage response to a moving hurricane. *J. Phys. Oceanogr.,* **24,** 233–260.

Sanford, T., P. Black, J. Haustein, J. Feeney, G. Forristal, and J. F. Price, 1987: Ocean response to a hurricane. Part 1: Observations. *J. Phys. Oceanogr.,* **17,** 2065–2083.

Shay, L. K., P. G. Black, A. J. Mariano, J. D. Hawkins, and R. L. Elsberry, 1992: Upper ocean response to Hurricane Gilbert. *J. Geophys. Res.,* **97,** 20 227–20 248.

Steffen, E., and E. D'Asaro, 2002: Deep convection in the Labrador Sea as observed by Lagrangian floats. *J. Phys. Oceanogr.,* **32,** 475–492.

Winters, K. B., and E. A. D'Asaro, 1996: Diapycnal fluxes in density stratified flows. *J. Fluid Mech.,* **317,** 179–193.

Wright, C. W., and Coauthors, 2001: Hurricane directional wave spectrum spatial variation in the open ocean. *J. Phys. Oceanogr.,* **31,** 2472–2488.